USM3D Analyses in Support of the NASA Langley 0.3-Meter Transonic Cryogenic Tunnel Test of Boundary-Layer Thickener Configurations

Michael D. Bozeman Jr.*, Alaa Elmiligui†, Gregory S. Jones‡, and William Milholen§
NASA Langley Research Center, Hampton, VA, Zip 23666

A wind tunnel test was performed in the 0.3-Meter Cryogenic Transonic Tunnel at the NASA Langley Research Center to investigate the impact of various boundary layer thickeners on the height and shape of the boundary layer on the aft portion of a semispan fuselage. The present work discusses USM3D analyses that were performed in support of the wind tunnel test. The results consisted of comparisons between USM3D and experimental data for the baseline configuration and two boundary layer thickening configurations. The comparisons considered surface pressure distributions, boundary layer profiles, and calculated boundary layer thicknesses. Additionally, a grid refinement study was performed for each of the three configurations, which illustrated general improvement in the comparisons with increasing grid refinement. Overall, the comparisons show favorable agreement between the USM3D predictions and the experimental data.

I. Nomenclature

BLT	=	Boundary Layer Thickener
C_P	=	pressure coefficient
h	=	grid refinement factor
L	=	length of wind tunnel model
M	=	Mach number
M_∞	=	freestream Mach number
N	=	grid dimension
P	=	static pressure
P_t	=	total pressure
$P_{t,\infty}$	=	freestream total pressure
r	=	maximum radius of wind tunnel model
R	=	flow solver residual
R_0	=	flow solver residual at first iteration
Re	=	unit Reynolds number, $\frac{\rho U_\infty}{\mu}$
Re_L	=	Reynolds number based on length L, $\frac{\rho U_\infty L}{\mu}$
r_1, r_2	=	stretching factors for boundary layer cell growth
T_T	=	total temperature
u	=	velocity component in x-direction
u_∞	=	freestream velocity
U	=	velocity magnitude
U_{edge}	=	velocity magnitude at edge of boundary layer
x, y, z	=	coordinate axes
y^+	=	inner scaling for wall-normal direction
δ	=	boundary layer thickness
δ_1	=	distance normal to the surface for the first cell in the boundary layer

*Pathways Research Student Trainee, Configuration Aerodynamics Branch. Student Member AIAA.
†Senior Research Engineer, Configuration Aerodynamics Branch, AIAA Senior Member.
‡Senior Research Engineer, Configuration Aerodynamics Branch, AIAA Associate Fellow.
§Senior Research Engineer, Configuration Aerodynamics Branch, AIAA Senior Member.

δ_{99} = boundary layer thickness corresponding to 99% of the edge value
Δs = distance normal to the surface
Δs_{max} = maximum distance normal to the surface that data were taken in the experiment
γ = ratio of specific heats

II. Introduction

Boundary Layer Ingestion (BLI) has been proposed as a technology with the potential to decrease fuel burn. BLI configurations feature propulsion systems that are tightly integrated into the airframe such that the boundary layer, or a fraction of it, is ingested by the propulsor. In order to produce thrust, the propulsor must accelerate the flow to obtain an increase in velocity at the exit relative to the velocity of the ingested flow. The BLI concept is based on the observation that it is more efficient to accelerate a low momentum flow to freestream velocity than to accelerate freestream velocity inflow to higher velocity values. And since a BLI propulsor is ingesting the lower momentum boundary layer, a higher propulsive efficiency can potentially be obtained. Additionally, the tight integration between the propulsor and the airframe can potentially cause favorable changes to the pressure distribution on the airframe resulting in reduced drag. As a result of both the increased propulsive efficiency and reduction in airframe drag, recent studies have predicted that BLI configurations can provide a potential benefit ranging from 5 to 12% [1–3]. One notable BLI concept is the Single Aisle Turboelectric Aircraft Concept with Aft Boundary Layer ingestion (STARC-ABL) [3]. The STARC-ABL is a turboelectric concept that employs a full-annular BLI propulsor powered by two underwing-turbofans. An illustration of the STARC-ABL concept is provided in Figure 1.

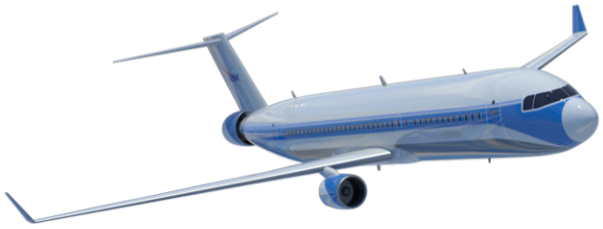

Fig. 1 Single-aisle transport aircraft with aft-boundary layer ingestion (STARC-ABL) [4].

NASA has invested in the STARC-ABL concept with the goal of quantifying the potential benefits of this configuration. As a first step, NASA will test a BLI model representative of the STARC-ABL concept at near flight Reynolds numbers in the National Transonic Facility (NTF). The NTF test will feature an unpowered tail-cone thruster consisting of a flow-through nacelle mounted on the aft-portion of the fuselage with mass flow plugs to achieve mass flow rates representative of flight conditions. The goals of the test are to both characterize the flow in the inlet and to quantify the propulsion-airframe integration (PAI) effects as a function of flight condition and the amount of boundary layer ingested by the BLI propulsor. However, the boundary layer thickness is fixed for a given geometry and flight condition. Boundary Layer Thickeners (BLTs) have been proposed as a potential method to allow for variations in boundary layer thickness for the upcoming test. Work performed by Otten [5] has illustrated the use of BLT pins for high-speed subsonic flow over a flat plate. For the present case, it is desired to employ BLTs on a circular cross-section representing the STARC-ABL afterbody for high speed subsonic flows. NASA has conducted a series of wind tunnel tests to investigate the ability of BLTs to achieve the desired variation in boundary layer thickness. The tests were performed in the 0.3-Meter Transonic Cryogenic Tunnel at the NASA Langley Research Center. The BLTs considered included eight pin configurations as well as six ramp configurations. This paper will briefly discuss the experiments and provide detailed results from CFD analyses that were performed in support of the 0.3-Meter test. An accompanying paper will discuss the experiments in greater detail [6].

III. Background

The basic idea for BLTs is to employ a mechanism to create a momentum deficit in the flow. Previous work demonstrated the use of BLT pins for both low speed and supersonic flows [7–10]. However, a variety of applications require full-scale boundary layers for subscale models subject to high speed subsonic flows. Based on this requirement, Otten performed a series of experiments to test the performance of BLTs for high speed subsonic flows [5]. The

experiments were conducted on a flat plate 2.08 m. long and 0.76 m. wide in the 6 ft. x 6 ft. pressure tunnel at the NASA Ames Research Center. The test conditions considered Mach and unit Reynolds numbers ranging from 0.6 to 0.9 and $6.57x10^6$/m to $13.14x10^6$/m, respectively. A total of five configurations were considered; the clean plate configuration and four pin configurations. An illustration of these configurations is provided in Figure 2.

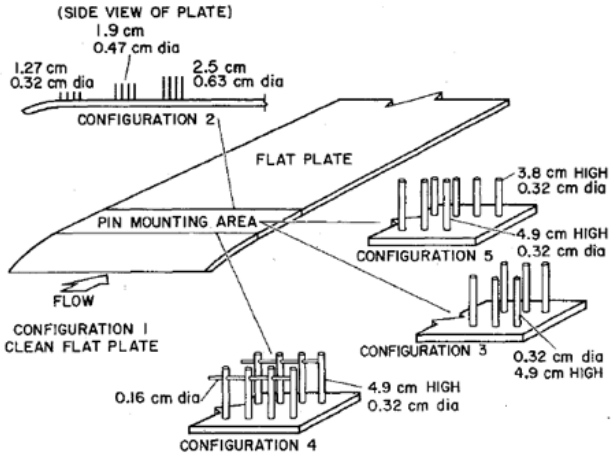

Fig. 2 Pin configurations considered by Otten [5].

For the described experiments, the BLT pins were designed for two purposes; to achieve both a desired increase in boundary layer thickness and a boundary layer profile corresponding to a power law with a prescribed exponent. The desired boundary layer thickness was defined by relating the increase in momentum thickness to the added drag resulting from the pins. The shape of the boundary layer was assumed to be a function of the distribution of the BLT pins. An example of the results obtained from this experiment are provided in Figure 3.

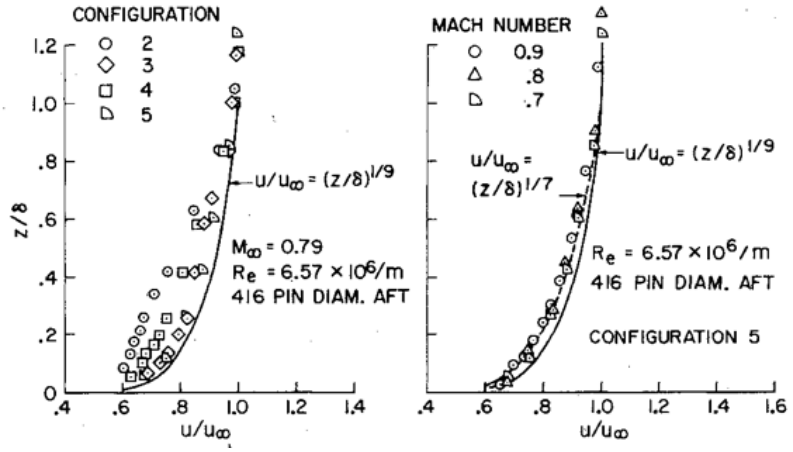

Fig. 3 Measured boundary-layer velocity profiles for pin configurations [5].

The results in Figure 3 show that all of the BLT configurations were approximately able to provide the desired boundary layer thickness. However, only Configuration 5 was able to provide a profile resembling a power law. The results also illustrate an insignificant effect of Mach number on the boundary layer profiles for Configuration 5. Finally, the results illustrate that the boundary layer resulting from Configuration 5 resembles a power law with an exponent of 1/7. This is an important result and illustrates the influence of the pin distribution on the resulting boundary layer profile. For more details about the experiments that were performed and the results, the reader is encouraged to see the original publication [5].

The present work is an extension of the work of Otten for a circular cross-section having a pressure gradient representative of a typical commercial transport afterbody. The results will provide insight into the variation in boundary

layer thickness and profile for a variety of BLT configurations. This insight will be used to design BLTs for the upcoming wind tunnel test of the shortened BLI configuration. Additionally, the results will provide a useful data set that can be used for validation of CFD codes.

IV. 0.3-Meter Wind Tunnel Test

This section will provide an overview of the 0.3-Meter Wind Tunnel Test including descriptions of the wind tunnel model, instrumentation, BLT configurations, testing facility, and test matrix. The primary focus of this paper is the CFD analyses that were performed in support of the 0.3-Meter test. As such, the experiments are only briefly described here. The reader is encouraged to refer to the accompanying paper for a more in-depth discussion of the experimental methods [6].

A. Model Geometry and Instrumentation

The model used for 0.3-Meter test consisted of three primary configurations. These configurations correspond to the top, side, and bottom views of the full configuration. This was accomplished by employing a removable aft section. An illustration of the model is provided in Figure 4.

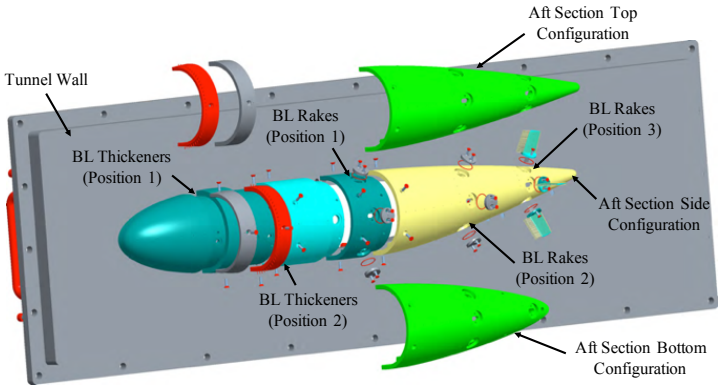

Fig. 4 Wind-tunnel model illustration with model changes included.

Figure 4 shows the three aft model sections along with the other various configurations that were available for testing. The other configurations include two positions for the BLTs and three positions for the boundary layer rakes. These combinations result in a total of 18 unique model configurations enabling the boundary layer measurements to be taken at three axial locations for the top, side, and bottom views and for two different axial locations for the BLTs. The model instrumentation for this experiment consisted of a combination of static pressure ports on the surface of the model and boundary layer rakes. Illustrations of the locations of the static pressure ports and boundary layer rakes are provided in Figures 5 and 6.

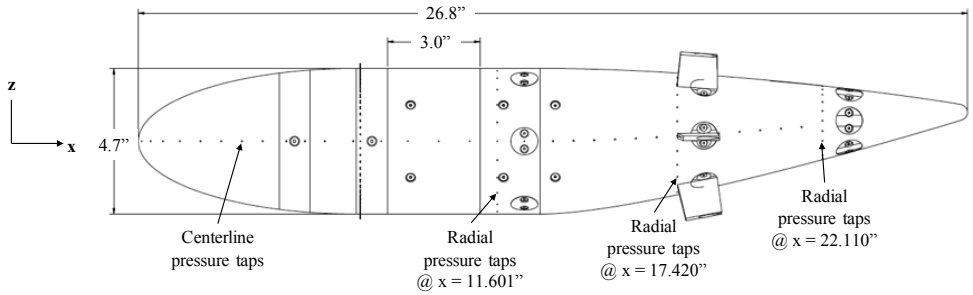

Fig. 5 Side-view illustration of static pressure taps.

Probe	Z (inches)
1	0.019
2	0.051
3	0.085
4	0.121
5	0.160
6	0.203
7	0.250
8	0.307
9	0.364
10	0.433
11	0.515
12	0.616
13	0.746
14	0.929
15	1.241

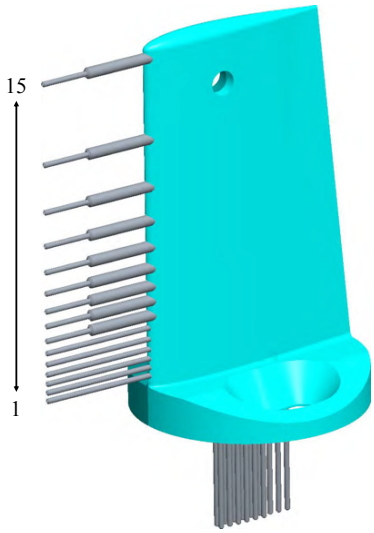

Fig. 6 Boundary layer rake probe locations.

Note that the focus of this paper is on the configuration consisting of the top view aft section and the boundary layer rakes and BLTs in their most aft locations (Position 3 and Position 2), respectively.

B. BLT Configurations

The test considered 14 BLTs in addition to the baseline model with no devices. The goal was to create a database that would allow for an assessment of the impact of the various configurations on the boundary layer height and shape. The selected BLTs included 7 pin configurations and 7 ramp configurations. The pin configurations include differences in pin height, number of rows, density of pins, and offset of pins between rows. Note that the pin diameter was fixed at 0.03125 inches for all pin configurations. For the ramp configurations, the variations include forward vs. backward facing ramps as well as ramp height. The configurations are briefly described in Table 1.

Table 1 BLT configurations.

Series	Description	Front Row Height (in)	Aft Row Height (in)
1	Baseline	0.0000	0.0000
2	Two row, same height	0.1290	0.1290
3	Two row, variable height	0.2580	0.2002
4	Single row	0.1500	N/A
5	Forward facing ramp	0.0500	N/A
6	Aft facing ramp	0.0500	N/A
7	Forward facing ramp	0.0300	N/A
8	Otton height	0.4300	0.3336
9	Aft facing ramp	0.0300	N/A
10	Single row	0.4530	N/A
11	Two row, variable height, high density	0.2580	0.2002
12	Otton height, high density	0.4300	0.3336
13	Forward facing ramp	0.1075	N/A
14	Forward facing ramp	0.1775	N/A
15	Forward facing ramp	0.0825	N/A

Note that this paper focuses on Series 1, 5, and 11. These configurations were chosen to represent the case of no BLT along with both a pin and ramp configuration. Illustrations of BLTs corresponding to Series 5 and 11 are provided in Figures 7 and 8. The results for the discussed configurations are provided in Section VI.

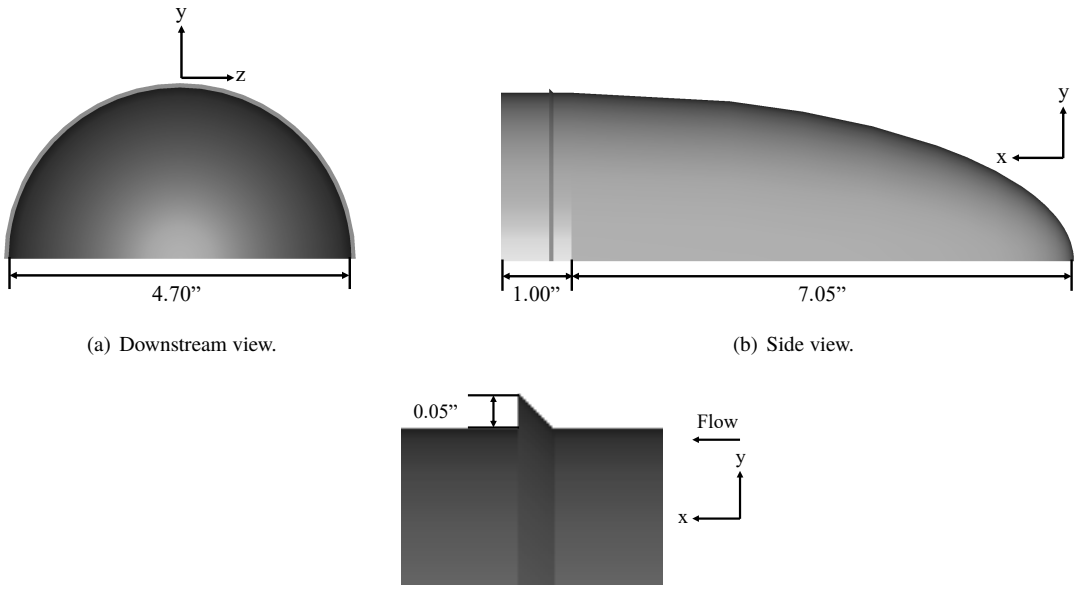

(a) Downstream view.

(b) Side view.

(c) Zoomed-in view of forward facing ramp.

Fig. 7 Series 5 - forward facing ramp.

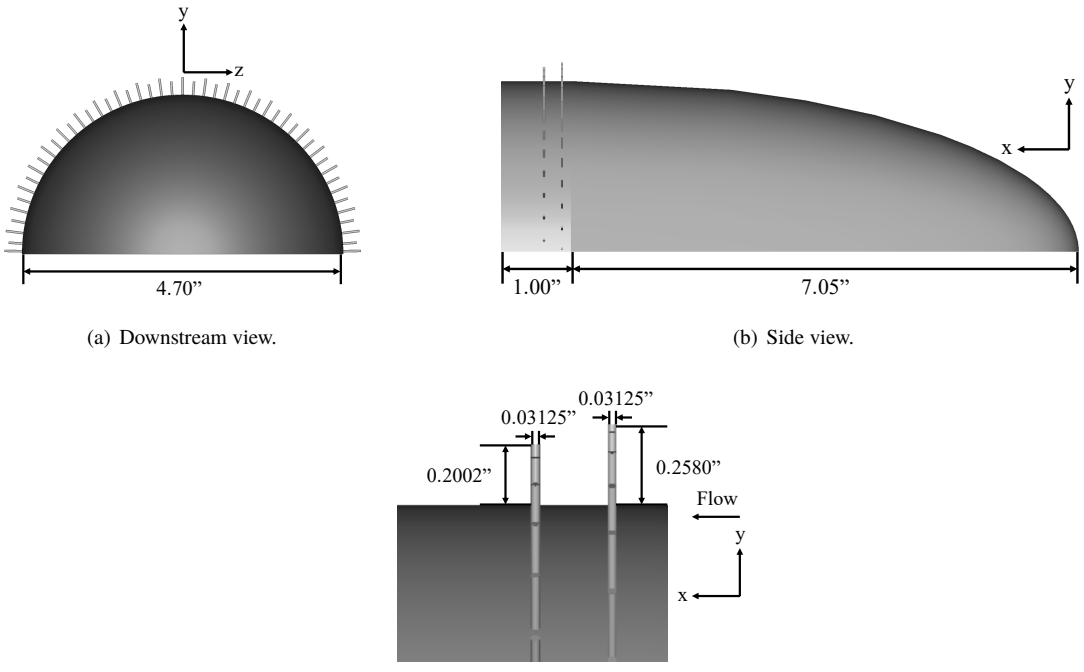

(a) Downstream view.

(b) Side view.

(c) Zoomed-in view of pins.

Fig. 8 Series 11 - two row, variable height, high density.

C. 0.3-Meter Transonic Cryogenic Tunnel at NASA Langley Research Center

The Langley 0.3-Meter Transonic Cryogenic Tunnel has a test section with a 13 inch x 13 inch cross-section and measuring 70.38 inches in length [11, 12]. The tunnel has been used to test airfoil sections as well as a variety of other configurations. It is capable of providing unit Reynolds numbers up to $100x10^6$ per foot and Mach numbers ranging from 0.1 to 0.9. Also, the facility is capable of running with both air and gaseous nitrogen to provide a broad range of test conditions. One notable feature of the 0.3-Meter tunnel is the adjustable walls, which allow the test section to be more streamlined and reduce the wall effects. An illustration of the 0.3-Meter tunnel is shown in Figure 9. For the present wind tunnel test, the tunnel wall settings were optimized to accomodate the semispan model. Two wall settings were employed for this test. Series 1 through 11 were tested using the wall setting illustrated in the Figure 10. This wall setting was found to result in significant wall effects. As a result, the wall position was changed for all tests performed after Series 11. This is discussed further in a companion paper [6]. The comparisons discussed in Section VI employ the wall setting provided in Figure 10.

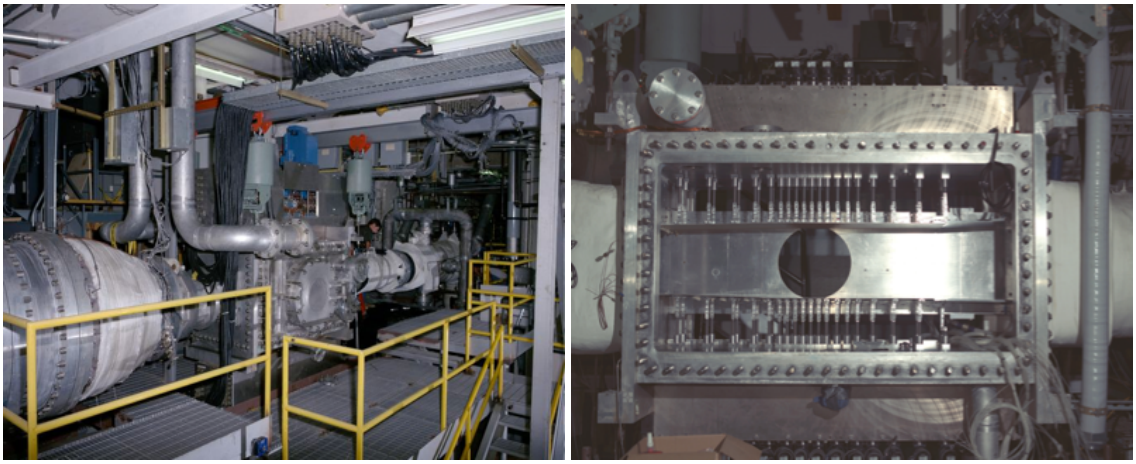

(a) External view. (b) Test section view with illustration of adjustable walls.

Fig. 9 0.3-Meter Transonic Cryogenic Tunnel at NASA Langley Research Center.

D. Test Matrix

The test matrix covered a range of conditions including Mach numbers ranging from 0.2 to 0.8 and Reynolds numbers ranging from $9.03x10^6$ to $58.62x10^6$. The test matrix for this test is outlined in Table 2.

Table 2 0.3-Meter test matrix.

Re_L (millions)	Pressure (psi)	T_T (°F)	Mach Number
9.03	14.70	80	0.2-0.7, by 0.1, 0.75, 0.8
27.05	44.10	-	-
45.02	73.50	-	-
45.11	51.02	-50	-
58.62	66.35	-	-

Note that not all conditions were run for each BLT configuration. For the present work, the experiments have been performed for one model configuration and 15 BLT configurations including the baseline. Additionally, the baseline configuration test points were repeated for the updated wall configuration. The resulting database consists of 615 total data points.

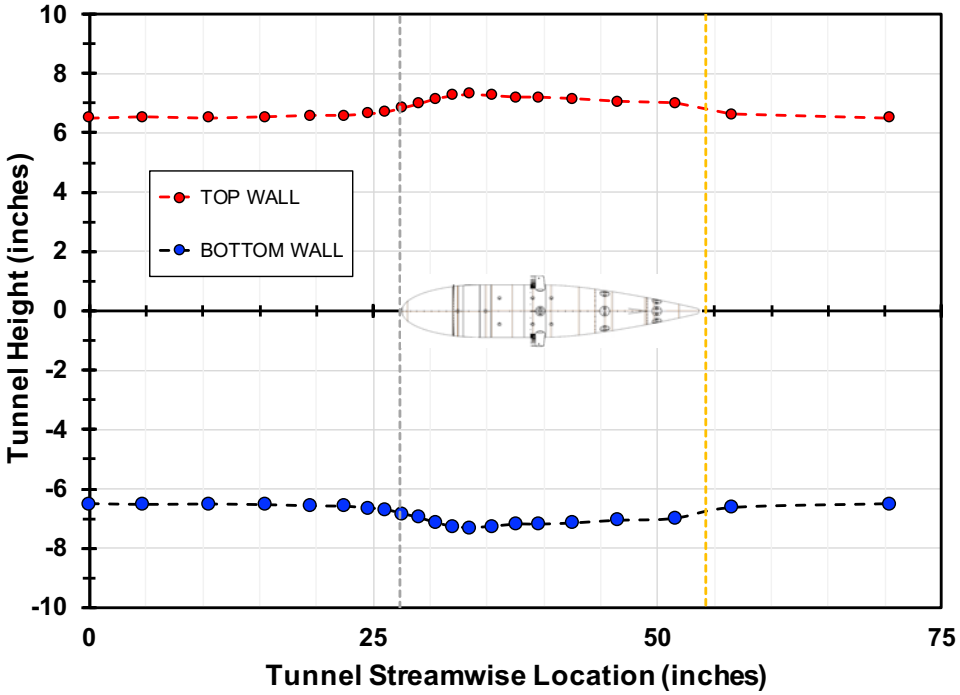

Fig. 10 Optimized wall position for semispan fuselage model.

V. Computational Methods

In this section, the computational methods used for the analyses of Series 1, 5, and 11 are discussed. The discussion includes a brief overview of the grid development, flow solver, and the boundary conditions employed for this work.

A. Computational Grids

To allow for comparisons between the wind tunnel results and CFD, a series of viscous grids were created for each of the series using the Heldenmesh™ v3.03 grid generation software [13]. Heldenmesh™ is an unstructured grid generator developed by the Helden Aerospace Corporation that utilizes multithreading for the rapid generation of both tetrahedral and mixed-element grids. Heldenmesh™ requires proper geometry definition prior to grid generation. Once the geometry definition is provided, Heldenmesh™ allows the user to specify the desired resolution of the surface grid through a series of inputs. This process is fairly automated depending on the complexity of the geometry, as well as the user preferences. Note that GridTool was used to obtain the geometry definition required for Heldenmesh™to generate grids for the BLT configurations. GridTool is available as part of the TetrUSS software package developed by the NASA Langley Research Center [14, 15]. It allows for a variety of geometry operations including geometry cleanup, source definition, and boundary condition specification.

For this work, the tunnel walls were modeled in their deformed state along with the semispan model mounted to the wall of test section. This was necessary based on the observation that the tunnel walls have a nonnegligible impact on the measured pressures, as discussed in Jones et al. [6]. Since the grids were to be used for a range of Reynolds and Mach numbers, the initial wall spacing was determined based on a desired y^+ of 1 at the most limiting condition provided in Table 2 corresponding to Mach and Reynolds numbers of 0.8 and 58.62 million, respectively. The resulting grid was designated as the coarse grid. An illustration of the coarse grid for the baseline configuration is provided in Figure 11.

Note that the grid resolution for each series varied as a result of the geometrical differences associated with the presence of the BLTs. For each series, the coarse grid was generated with an average spacing of 0.01 inches to resolve the BLT. The resulting differences in grid resolution are illustrated in Figure 12 for Series 1, 5, and 11. Note that an average spacing of 0.01 inches resulted in roughly 15 points along the axial distance of the ramp for Series 5 and 10 points around the circumference of the pins for Series 11. The differences between the grids were limited to the vicinity of the BLT with the remainder of the computational domains being identical between the series. Additionally, medium, fine, and extra fine grids were generated to assess the sensitivity of the solutions to the grid density. Note that due to the

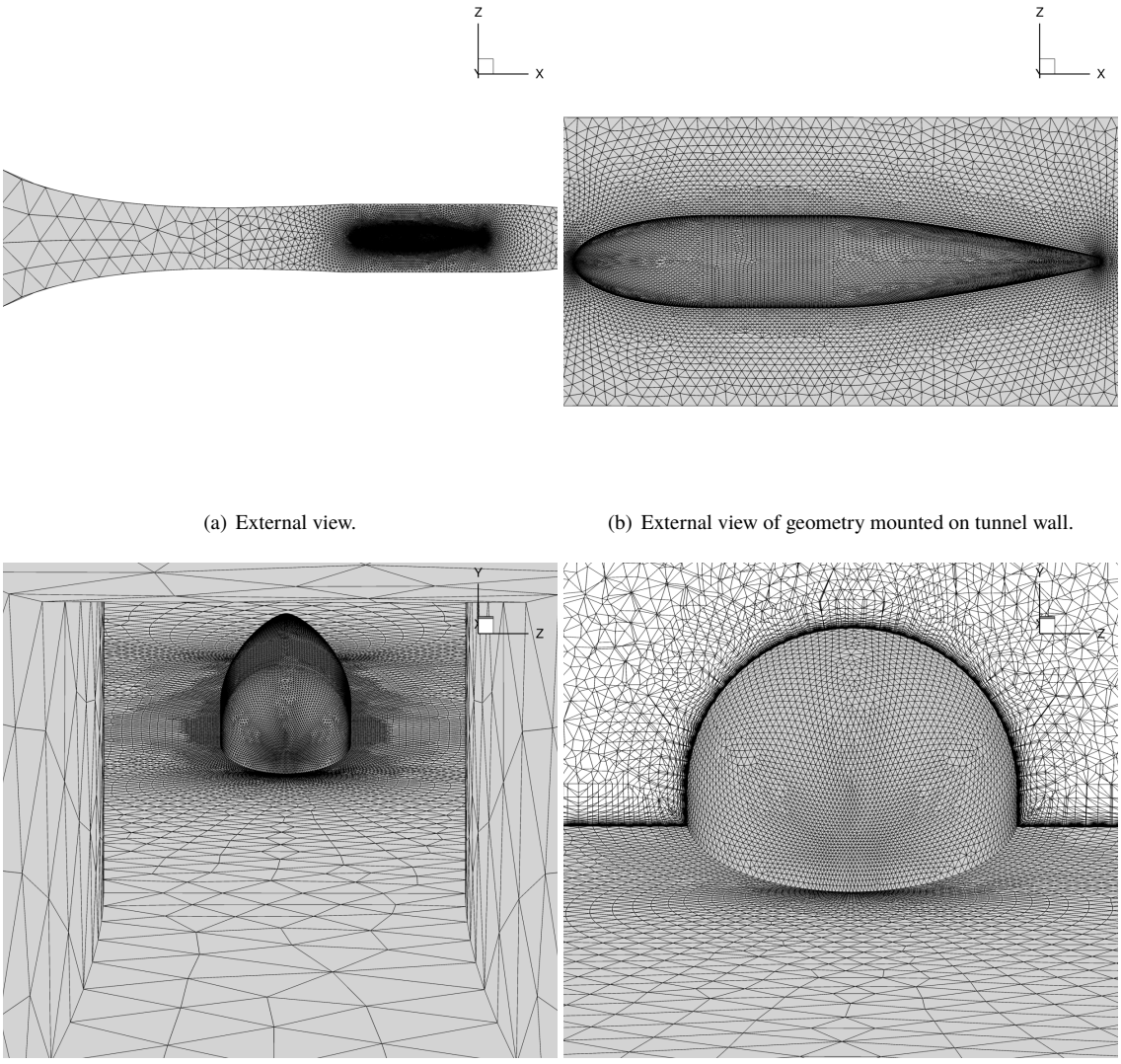

(a) External view.

(b) External view of geometry mounted on tunnel wall.

(c) Downstream view of model in tunnel.

(d) Downstream view of boundary layer growth on surface.

Fig. 11 Coarse grid for baseline case with tunnel included.

differences in grid resolution resulting from the BLTs, the grid sensitivity study was performed for Series 1, 5, and 11; requiring a total of 12 grids.

To create the grids for the grid sensitivity study, HeldenMesh™ provides a user-defined refinement factor, h, to allow for global changes in grid resolution. The grid refinement factor can be used to either refine or coarsen the initial grid. For this work, the coarse grid was sequentially refined to provide a factor of 2 difference in the number of cells between successive grids. Note that the refinement factor, h, is not directly applied to the initial wall spacing or growth rate of the boundary layer cells in HeldenMesh™. In an effort to obtain a series of uniformly scaled grids, the refinement factor, h, was also manually applied to scale the initial wall spacing and growth rate. The grid spacing normal to the surface in the boundary layer is defined by Equation 1 in HeldenMesh™, where δ_i represents the distance normal to the wall for node i and r_1 and r_2 are stretching factors that define the rate at which the spacing between adjacent cells increases with distance from the wall. The inital wall spacing, δ_1, was scaled linearly by the refinement factor, h, using Equation 2. Then, each of the stretching factors, r_1 and r_2, were scaled using a linear scaling in the log-space as shown in Equation 3, which is consistent with the method employed by Park et al. [16]. The sizes of the resulting grids for Series 1, 5, and 11 are provided in Table 3.

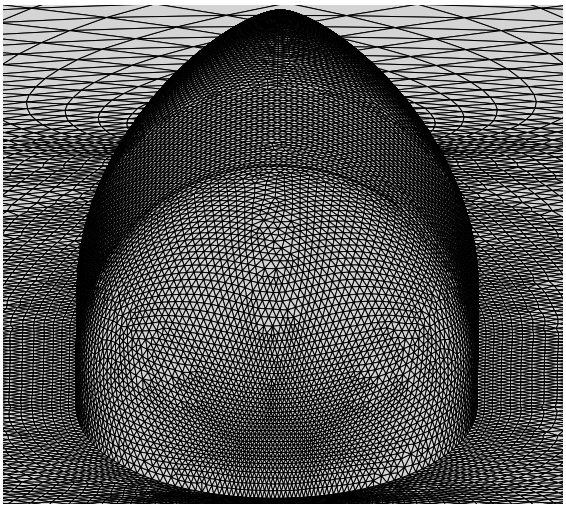

(a) Series 1 - baseline

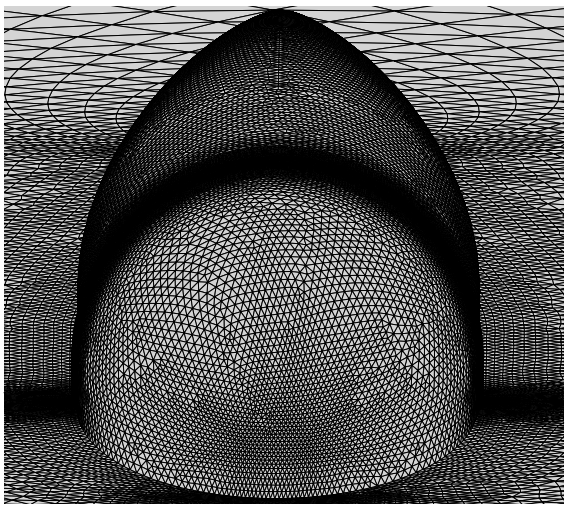

(b) Series 5 - forward facing ramp

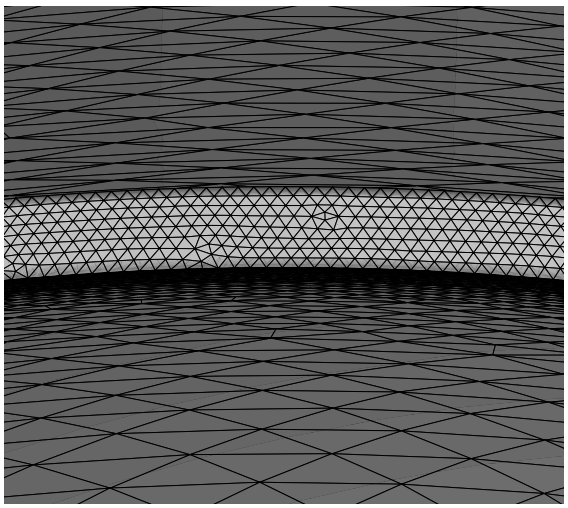

(c) Series 5 - zoomed in, downstream view of ramp

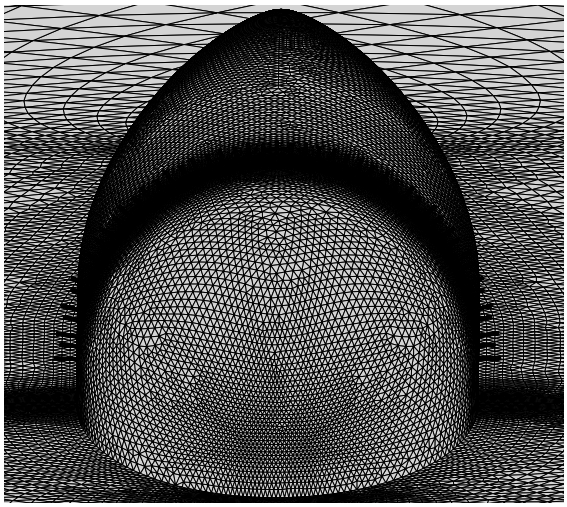

(d) Series 11 - two row, variable height, high density

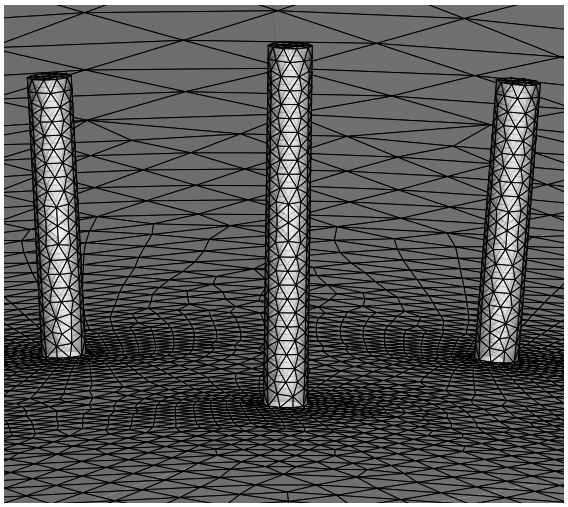

(e) Series 11 - zoomed in, downstream view of pins

Fig. 12 Illustration of resolution differences caused by the presence of BLTs.

$$\delta_{i+1} = \delta_i(1 + r_1(r_2 + 1)^i)^i \tag{1}$$

$$\delta_1(h) = \delta_1(h = 1)h \tag{2}$$

$$r_{1,2}(h) = e^{hln(1+r_{1,2}(h=1))} - 1 \tag{3}$$

Table 3 Grid resolutions for Series 1, 5, and 11.

		h	δ_1 (inches)	r_1	r_2	Cells (millions)
Series 1	Coarse	1.00	3.00×10^{-5}	0.150	0.020	5.00
	Medium	0.725	2.18×10^{-5}	0.107	0.014	10.1
	Fine	0.548	1.64×10^{-5}	0.080	0.011	20.0
	Extra Fine	0.421	1.26×10^{-5}	0.061	0.008	39.9
Series 5	Coarse	1.00	3.00×10^{-5}	0.150	0.020	11.0
	Medium	0.719	2.16×10^{-5}	0.106	0.014	22.0
	Fine	0.529	1.59×10^{-5}	0.077	0.011	44.1
	Extra Fine	0.397	1.19×10^{-5}	0.057	0.008	87.8
Series 11	Coarse	1.00	3.00×10^{-5}	0.150	0.020	14.1
	Medium	0.713	2.14×10^{-5}	0.105	0.014	27.9
	Fine	0.518	1.55×10^{-5}	0.075	0.010	55.8
	Extra Fine	0.386	1.16×10^{-5}	0.055	0.008	112.6

B. USM3D Flow Solver

The flow solver used for the computational analyses is the USM3D flow solver. USM3D is an unstructured, cell-centered Reynolds-averaged Navier-Stokes (RANS) flow solver developed at the NASA Langley Research Center [17]. The current release at the time of this writing required all tetrahedral grids. However, future releases of the USM3D solver will also allow for mixed-element grids [18]. USM3D employs upwind schemes for the inviscid flux computations with a variety of flux schemes and turbulence models available. For the present study, the Spalart-Allmaras (SA) one equation model was used with the Quadratic Constitutive Relation (QCR) for the Reynolds stresses. The inviscid fluxes were computed using the Harten-Lax-van Leer-Contact (HLLC) scheme. Also, all of the simulations were performed as steady with CFL ramping from 1 to 30 for accelerated convergence.

C. Boundary Conditions

The boundary conditions for the 0.3-Meter tunnel simulations included a no-slip constraint on the tunnel walls and model surface, prescribed total pressure and temperature at the tunnel inflow boundary, and a prescribed back pressure at the tunnel outflow boundary. Note that the back pressure at the outflow was an unknown quantity. However, the Mach number in the test section was known from the experiment. To account for this, a proportional controller was used to adjust the back pressure at the outflow boundary to match the target Mach number at the test section based on the given total conditions at the tunnel exit and a measured static pressure on the tunnel wall, which is consistent with the method used to set the Mach number in the experiment. At each controller iteration, both the total pressure at the tunnel entrance and the static pressure on the wall just upstream of the test section were sampled. The relationship between the static pressure, total pressure, and Mach number used for this work is given by the isentropic flow expression provided

in Equation 4. The final expression used for the controller, provided in Equation 5, was obtained by solving Equation 4 for the Mach number. Then, the sampled static pressure and total pressure values were used along with Equation 5 to calculate the Mach number for each controller iteration and the back pressure at the outflow boundary was updated. For this work, the back pressure was updated every 500 iterations.

$$\frac{P}{P_t} = \left(1 + \frac{\gamma - 1}{2} M^2\right)^{-\frac{\gamma}{\gamma - 1}} \tag{4}$$

$$M = \sqrt{\frac{2}{\gamma - 1}\left(\left(\frac{P}{P_t}\right)^{-\frac{\gamma - 1}{\gamma}} - 1\right)} \tag{5}$$

VI. Results

This section discusses the results of the USM3D analyses performed for Series 1, 5, and 11. Note that all of the results provided in this paper correspond to Reynolds and Mach numbers of 58.45×10^6 and 0.75, respectively. The discussion includes the convergence behavior and criteria used for the USM3D simulations, comparisons to experimental data, and the impact of grid resolution on the predictions.

A. Convergence

The convergence criteria used for this work was a minimum of three orders reduction in the magnitude of the flow residuals. Additionally, the difference between the calculated Mach number at the entrance to the test section and the target Mach number was required to approach zero. This second requirement results from the iterative back pressure at the tunnel exit that was employed to match a target Mach number at the entrance to the test section, which was discussed in Section V.C. For this work, the convergence criteria was generally met by 20,000 solver iterations. An illustration of the convergence behavior for the baseline configuration and coarse grid is provided in Figure 13.

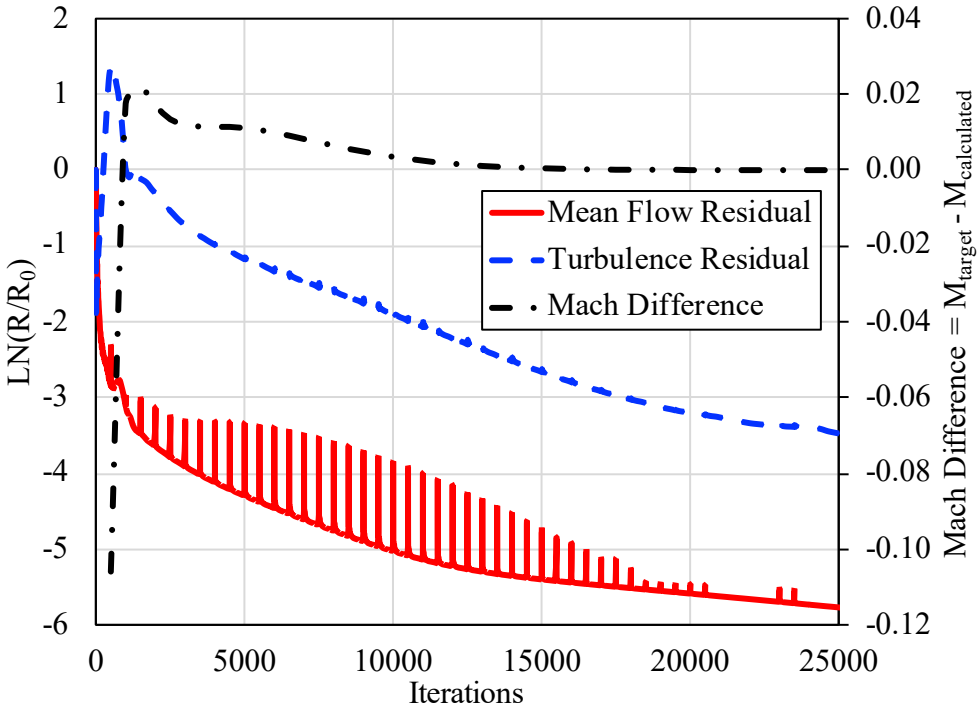

Fig. 13 Convergence history for baseline configuration.

The results show that the mean flow residual is reduced by three orders of magnitude within roughly the first 1,500 iterations. However, the turbulence residual requires significantly more iterations to meet the convergence criteria. Note that the spikes observed in the residuals are the result of the iterative update to the back pressure at the tunnel exit. The results also show that the Mach number is within 0.01 of the target by roughly 5,000 iterations but then requires another 10,000 iterations to reach the target. The convergence behavior illustrated here was typical of all of the simulations performed for this work with the exception of the number of iterations to meet the convergence criteria, which was observed to increase for increasing grid refinement.

B. Series 1 - Baseline Configuration

The first set of results discussed correspond to Series 1, which is the baseline configuration. As previously discussed, this configuration does not include a BLT. The comparisons provided for Series 1, therefore, assess the ability of USM3D to perform accurate predictions for the 0.3 Meter Tunnel with the semispan model installed. The following sections include incremental changes with the only difference being the presence of the BLTs. The results provided for each of the series include comparisons of the pressure coefficient at static ports along the centerline of the wind tunnel model and velocity and total pressure profiles in the boundary layer corresponding to the center boundary layer rake. Additionally, each of the comparisons include the USM3D predictions for the coarse, medium, fine, and extra fine grids that were discussed in Section V.A. The results for Series 1 are provided in Figures 14 through 17.

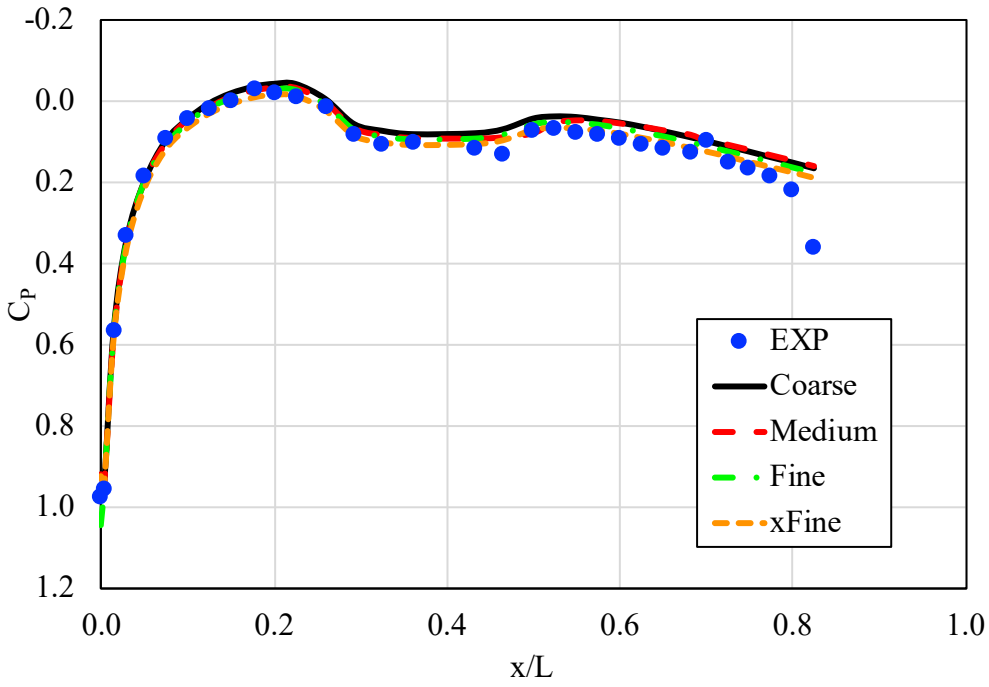

Fig. 14 Centerline pressure coefficient results for Series 1 ($Re_L = 58.45 \times 10^6$, $M = 0.75$).

The centerline pressure coefficient comparisons show favorable agreement between the experimental data and the USM3D flow solver. Note that the discrepancy shown for the most aft points are a result of interference that was observed between the boundary layer rake and the static pressure ports at that location. This interference is illustrated in Figure 15, which corresponds to the radial distribution of the pressure coefficient at the axial location corresponding to the location of the boundary layer rakes. The results show significant spikes at the location of the three rakes with better agreement near the edges. Another observation that can be made from Figure 14 is that the grid resolution does not appear to have a significant impact on the predicted pressure coefficient values. While refining the grid from coarse to extra fine does improve the agreement between USM3D and the experimental data, the differences between the grid resolutions are small.

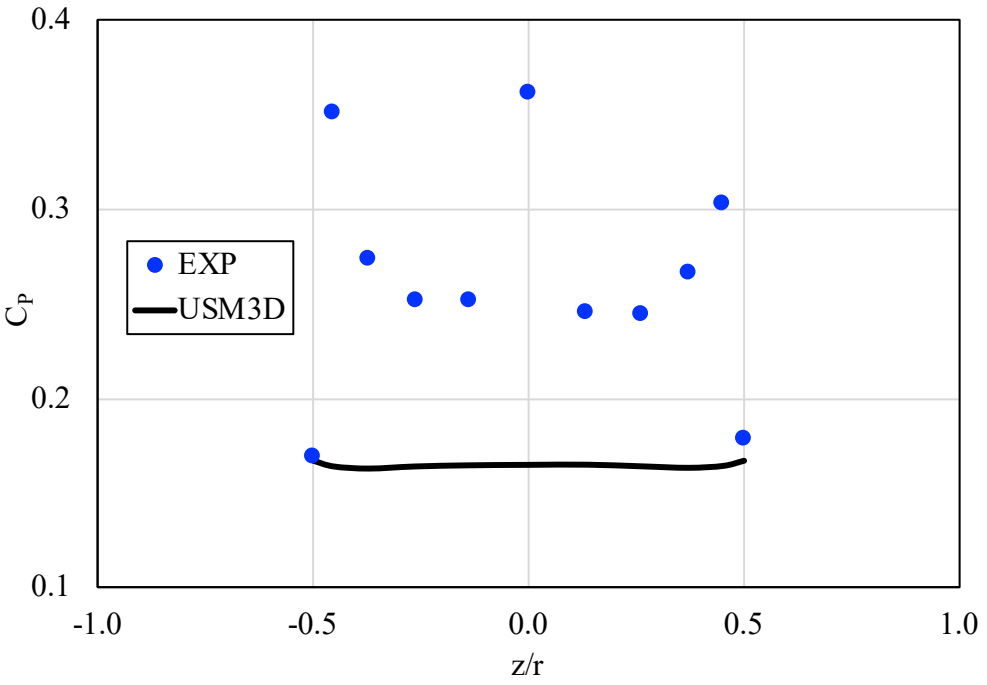

Fig. 15 Influence of boundary layer rake on the radial distribution of pressure coefficient on the model surface ($Re_L = 58.45 \times 10^6$, $M = 0.75$).

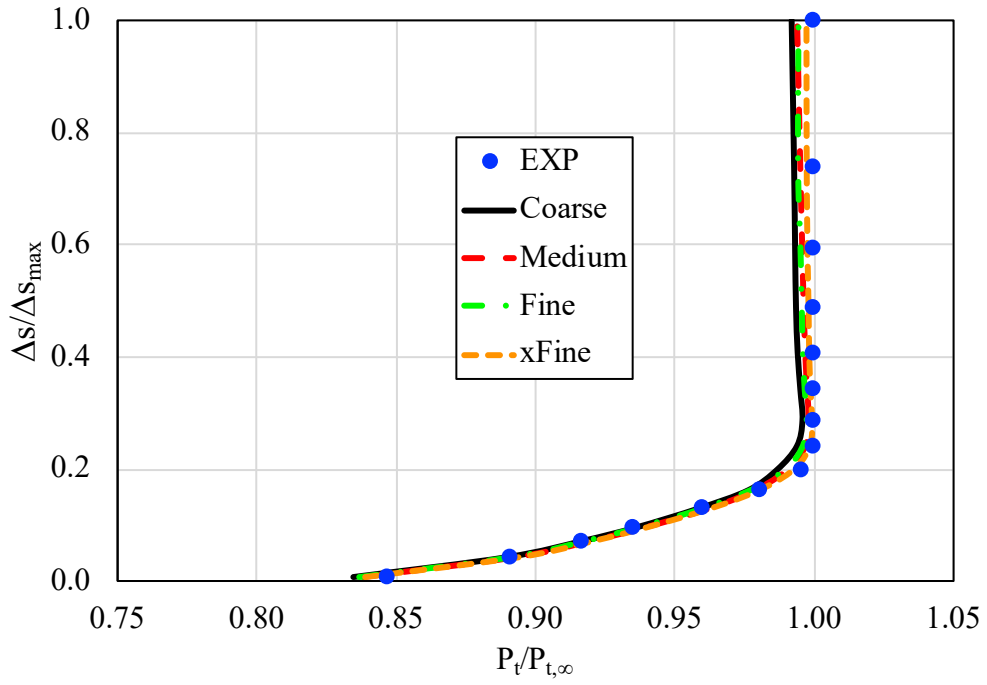

Fig. 16 Total pressure profile comparisons at center rake for Series 1 ($Re_L = 58.45 \times 10^6$, $M = 0.75$).

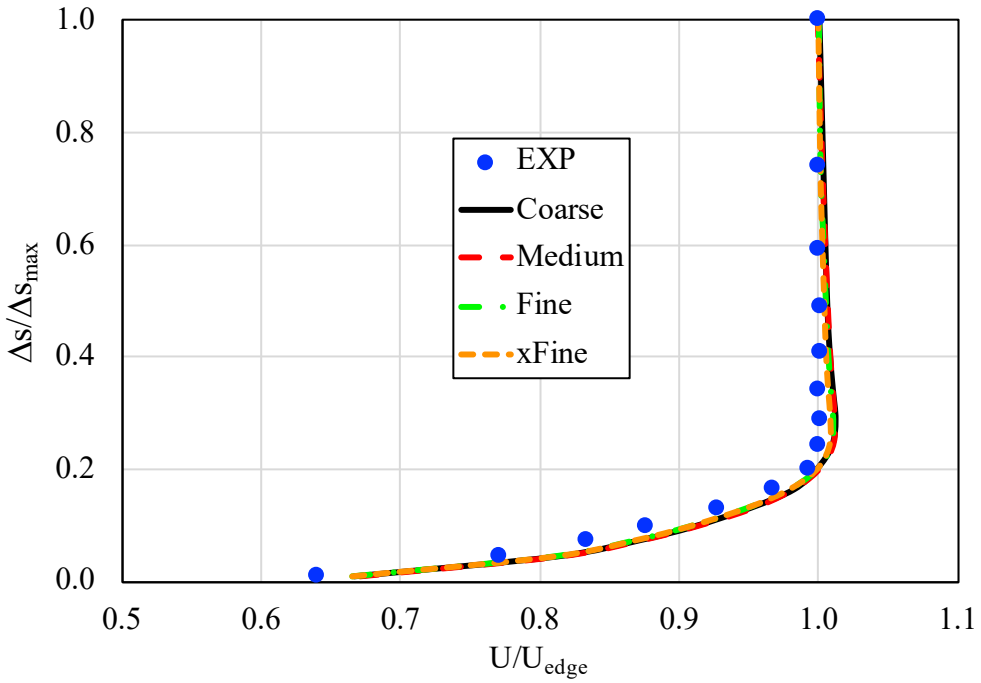

Fig. 17 Velocity profile comparisons at center rake for Series 1 ($Re_L = 58.45 \times 10^6$, $M = 0.75$).

The boundary layer profiles for the total pressure and velocity are illustrated in Figures 16 and 17. Note that the velocity, U, profiles are normalized by the edge velocity, U_{edge}, which was taken to be the velocity farthest from the surface to allow for comparisons between the actual shape of the profiles. Also, the total pressure, P_t, profiles are normalized by the freestream total pressure, $P_{t,\infty}$, to illustrate both the shape and the differences in the total pressure losses with changes in grid resolution. Finally, the distance from the surface, Δs, is normalized by the maximum distance from the surface for the given boundary layer rake measurements, Δs_{max}. The total pressure profile comparisons provided in Figure 16 illustrate favorable agreement for Series 1. The results show that increasing the grid density results in a decrease in the total pressure losses in the tunnel and better agreement with the experimental data. However, similar to the centerline pressure coefficient results, the impact of grid density does not appear to be significant for the Series 1 predictions. The velocity profile comparisons illustrate some differences in the shape, but overall, the results appear to agree favorably. One interesting observation is that the USM3D predicted velocity profiles exhibit an overshoot where the value of U/U_{edge} is greater than 1 starting at a $\Delta s/\Delta s_{max}$ value of 0.2 and does not return to a value of 1 until roughly a $\Delta s/\Delta s_{max}$ value of 0.75. However, the experimental results do not exhibit this same behavior. Note that while the impact of grid resolution is relatively insignificant, the overshoot does appear to be decreasing in magnitude as the grid density increases. Another important note is that the velocity profiles were not measured in the experiment. The total pressure was measured using the pitot probes attached to the boundary layer rake. Then, using an average of the static pressures measured on the surface and the assumption of constant static pressure in the boundary layer, the total pressure data are used to compute the velocity profiles. However, as shown in Figure 15, the static pressures measured on the surface at the location where the boundary layer profiles were measured are influenced by the presence of the rake. This could result in some differences in the experimentally obtained velocity profiles and those predicted by USM3D.

The final results provided for Series 1, shown in Figure 18, compare the resulting boundary layer thickness as a function of grid density, where the grid density is plotted as the number of cells, N, raised to the -2/3 power. The boundary layer thickness was calculated using both the velocity and total pressure profiles for comparison. For the velocity profiles, the boundary layer thickness was calculated based on the location where the velocity ratio, U/U_{edge}, is equal to 0.99. Similarly, the boundary layer thickness for the total pressure profiles was calculated based on the location where the total pressure ratio, $P_t/P_{t,edge}$, is equal to 0.99. Note that while the profiles shown in Figure 16 are normalized by the freestream total pressure, the edge value was used to calculate the boundary layer thickness to mitigate the impact of total pressure losses on the predicted thicknesses. The results show that the calculated boundary layer thicknesses vary only slightly with grid density for Series 1 and are practically constant for the fine and extra fine grids. The maximum and minimum values predicted for the four grid refinements differ by roughly 0.007 inches, which

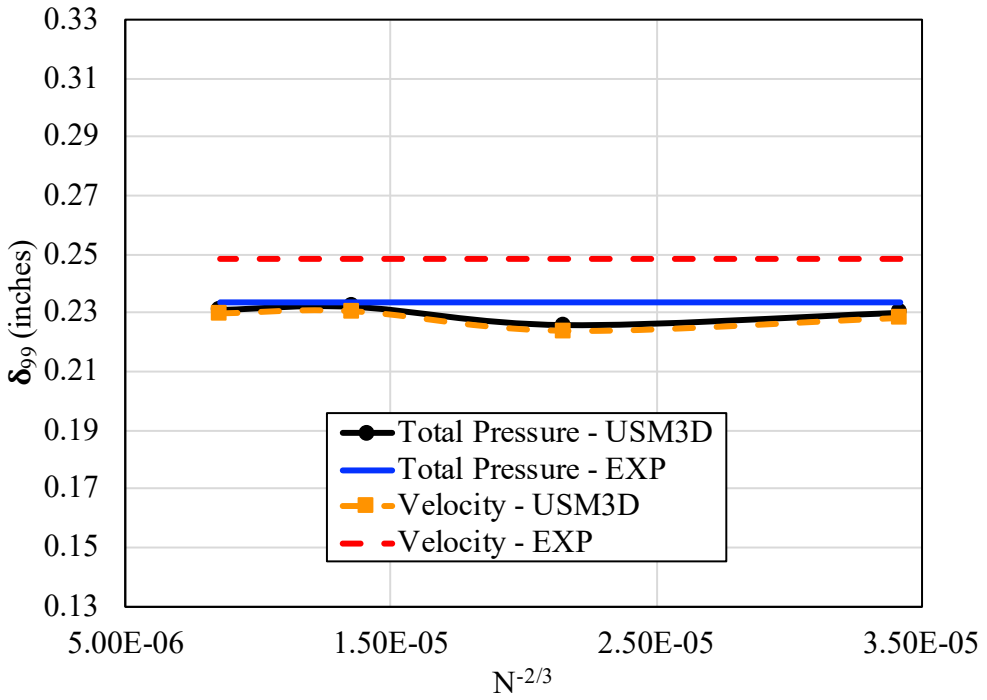

Fig. 18 Calculated boundary layer thickness comparisons for Series 1 ($Re_L = 58.45 \times 10^6$, $M = 0.75$).

is true for both the total pressure and velocity profiles. Also, the thickness values calculated using the total pressure profiles compare well between USM3D and the experiment with a maximum difference of 0.008 inches. However, the differences are much more significant for the values calculated using the velocity profiles with a maximum difference of 0.025 inches. This difference is a potential result of the interference of the boundary layer rake on the measured static pressures that was discussed previously. Overall, the USM3D results compare very well with the experimental results for Series 1.

C. Series 5 - Forward Facing Ramp Configuration

The comparisons between USM3D and the experimental data for Series 5 were conducted similarly to the comparisons performed for Series 1 in the previous subsection. The centerline pressure coefficient results obtained from USM3D as a function of grid refinement are compared to the experimentally obtained values in Figure 19. The centerline pressure coefficient results show favorable agreement between the experiment and USM3D. Once again, the impact of grid refinement appears to be minimal for the grids considered in this paper. The forward facing ramp increases the momentum deficit of the flow by causing the flow to separate and then reattach downstream of the ramp. As the flow approaches the ramp, it experiences a strong adverse pressure gradient. Then, the USM3D predictions show a sudden decrease at the end of the ramp, which corresponds to flow separation behind the ramp. Finally, the results show that the flow reattaches just downstream of the ramp. Comparing to the experimental values, the separation point appears to be further downstream relative to the USM3D predictions. However, it is difficult to know exactly what is taking place due to the sparsity of the measured values in this region.

The total pressure profile comparisons provided in Figure 20 show differences close to the surface with better agreement farther away from the surface. The total pressure losses in the tunnel decrease with increasing grid refinement and the impact of grid resolution appears to be more significant for Series 5 relative to Series 1. Also, the differences close to the surface become smaller with increasing grid resolution. However, it does appear that the solution is not grid converged and could potentially benefit from further refinement. The velocity profile comparisons provided in Figure 21 show slightly better agreement close to the surface with larger differences further away, which is the opposite trend observed for the total pressure profiles. Similar to the Series 1 results, the velocity profile predictions from USM3D exhibit an overshoot, which is not present in the experimental values. Finally, the boundary layer thickness results are provided in Figure 22.

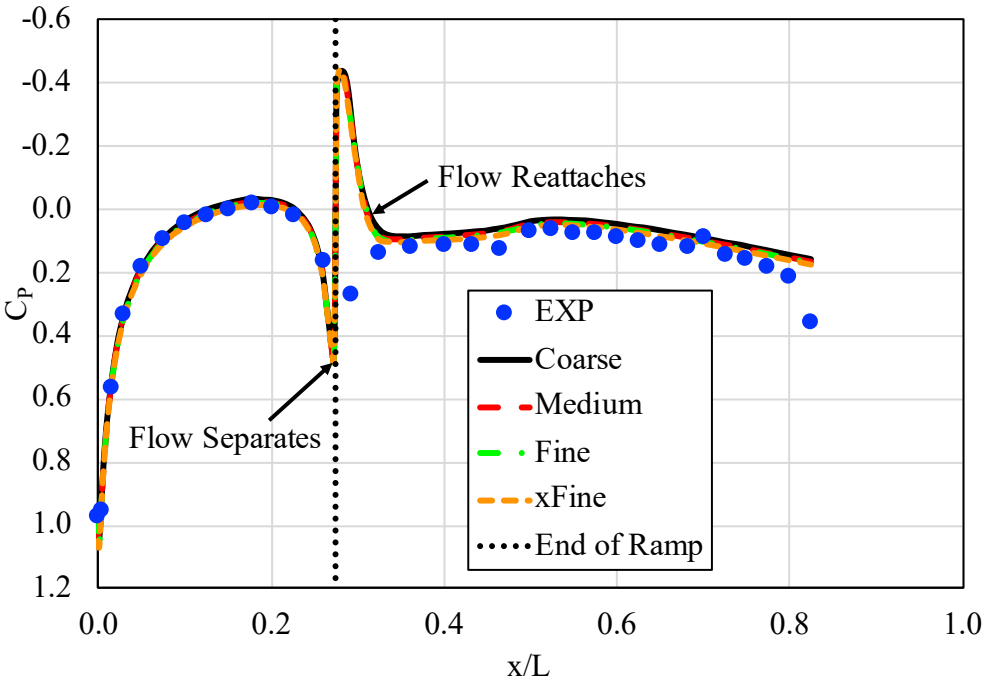

Fig. 19 Centerline pressure coefficient results for Series 5 ($Re_L = 58.45 \times 10^6$, $M = 0.75$).

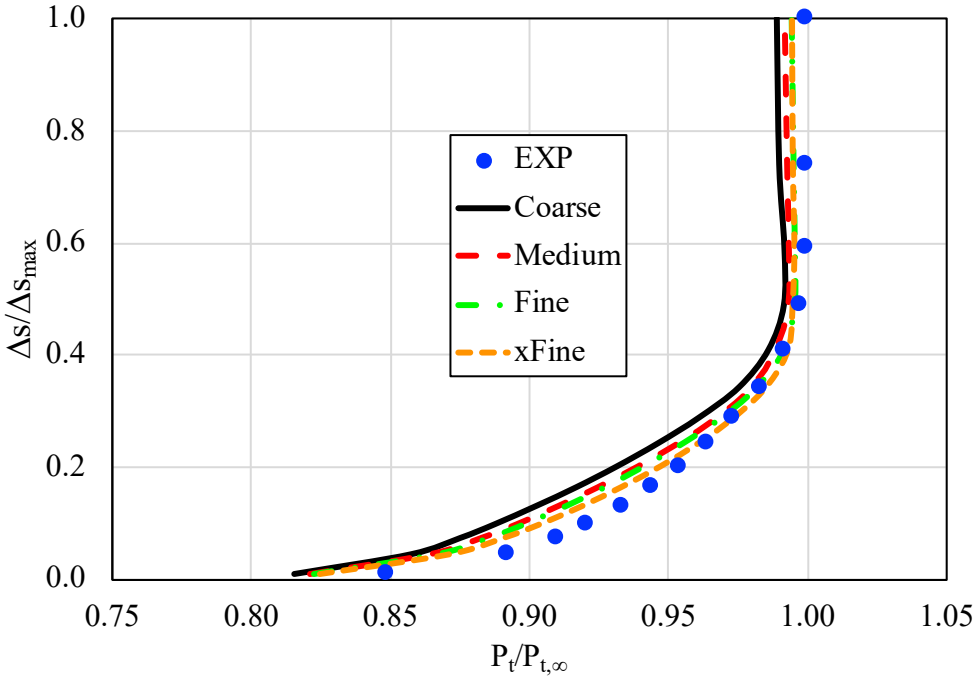

Fig. 20 Total pressure profile comparisons at center rake for Series 5 ($Re_L = 58.45 \times 10^6$, $M = 0.75$).

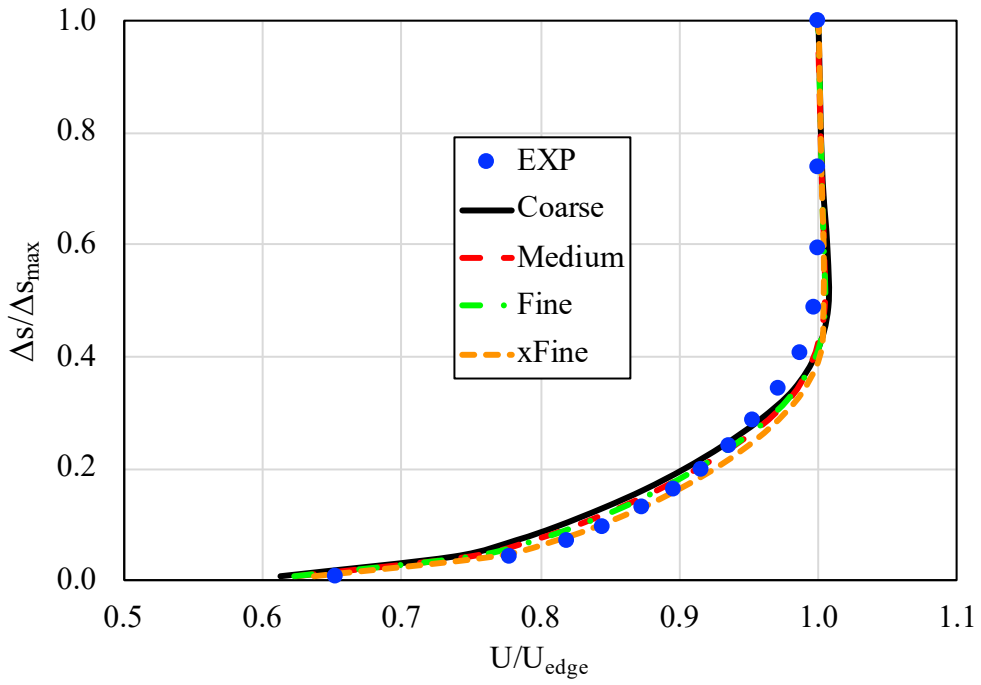

Fig. 21 Velocity profile comparisons at center rake for Series 5 ($Re_L = 58.45 \times 10^6, M = 0.75$).

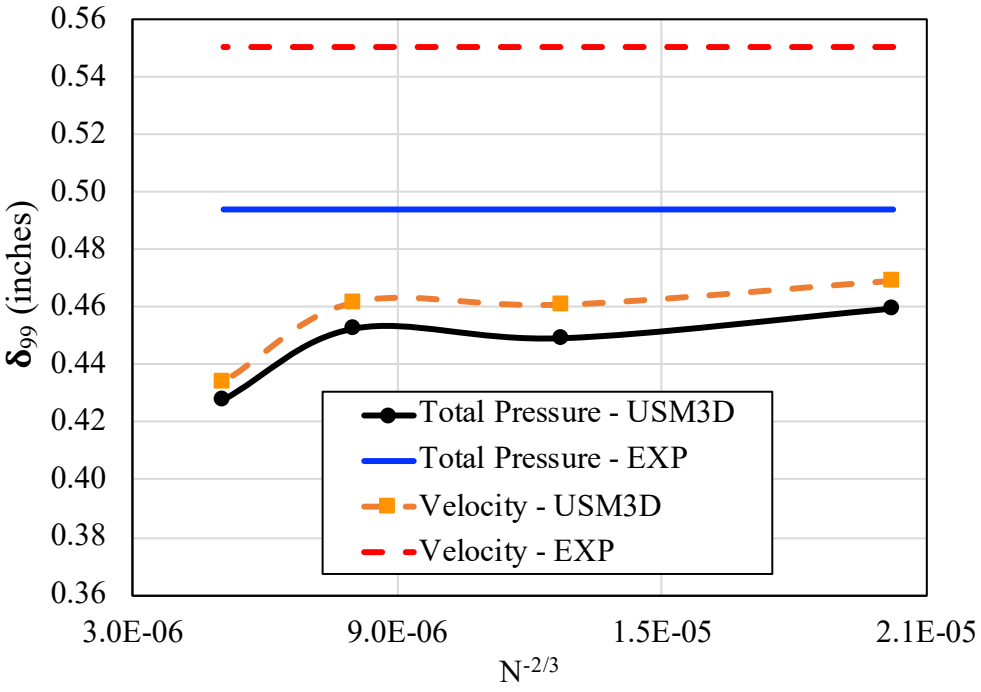

Fig. 22 Calculated boundary layer thickness comparisons for Series 5 ($Re_L = 58.45 \times 10^6, M = 0.75$).

The calculated boundary layer thicknesses, illustrated in Figure 22, show that the impact of grid sensitivity is fairly insignificant for the coarse, medium, and fine grids, with a maximum difference of 0.01 inches between the grid refinements. However, the thicknesses calculated for the extra fine grid exhibit large differences relative to the coarser grids. This is another indicator that further grid resolution is needed to make a complete assessment of the impact of grid density for Series 5. Finally, the results show that, again, the boundary layer thicknesses computed for the total pressure profiles agree more favorably to the experiment than the values obtained using the velocity profiles.

D. Series 11 - Two Row, Variable Height, High Density Pin Configuration

The final BLT configuration that will be discussed is the two row, variable height, high density pin configuration, also referred to as Series 11. The centerline pressure coefficient comparisons, provided in Figure 23, show favorable agreement between the experiment and USM3D with only limited influence of grid resolution for the grids considered in this paper. Similar to the forward facing ramp, the pin configuration increases the momentum deficit of the flow by causing the flow to separate and then reattach downstream of the pins. As the flow approaches the pins, it experiences an adverse pressure gradient. Then, the USM3D predictions show a sudden decrease in the pressure coefficient, which corresponds to flow separation. Finally, the results show that the flow reattaches just downstream of the pins. Comparing to the centerline pressure coefficient results for Series 5, the extent of the separated flow region is smaller for Series 11. Note that Series 11 consists of two rows of pins, which are staggered such that any axial slice of the surface will only pass through one row of pins. The centerline pressure coefficient values provided in Figure 23 pass through the first row of pins and between the second row. For a slice that passes through the second row of pins, the flow separation would be further aft relative to the results discussed in this section.

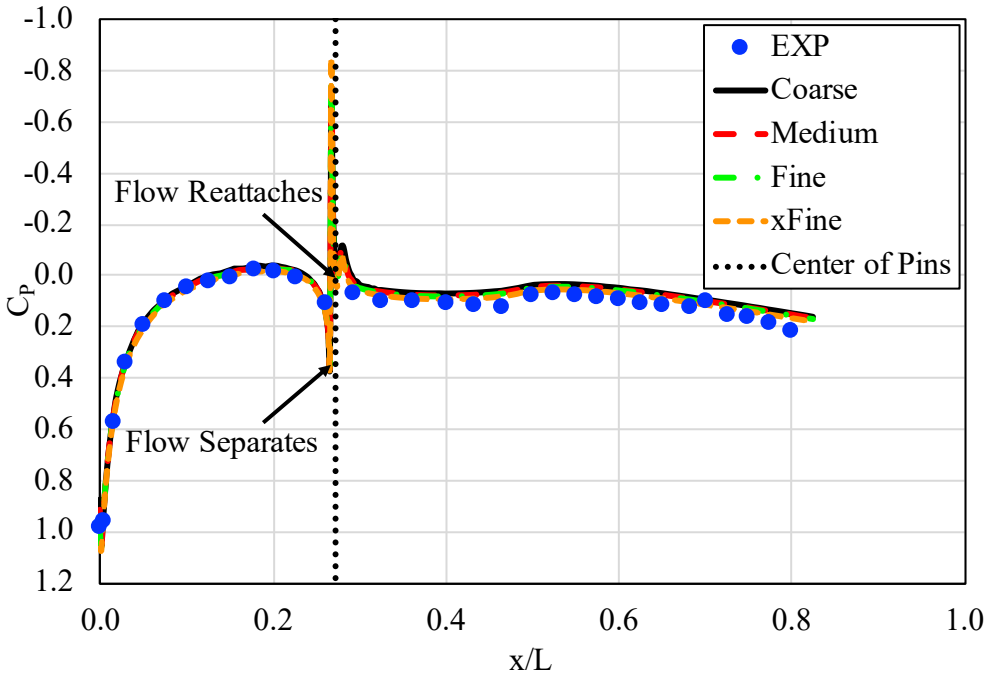

Fig. 23 Centerline pressure coefficient results for Series 11 ($Re_L = 58.45 \times 10^6$, $M = 0.75$).

Similar to the results discussed for Series 5, the total pressure profiles provided in Figure 24 show differences between the USM3D predictions and the experimental data close to the surface with better agreement further from the surface and decreasing total pressure losses with increasing grid resolution. The velocity profile comparisons in Figure 25 also show differences close to the surface with better agreement further from the surface. However, in this case, the shape of the velocity profiles predicted by USM3D better agree with the experiment relative to the total pressure profiles. This observation is interesting since the total pressure values are the measured quantities that would be expected to match better. Finally, the calculated boundary layer thicknesses are provided in Figure 26.

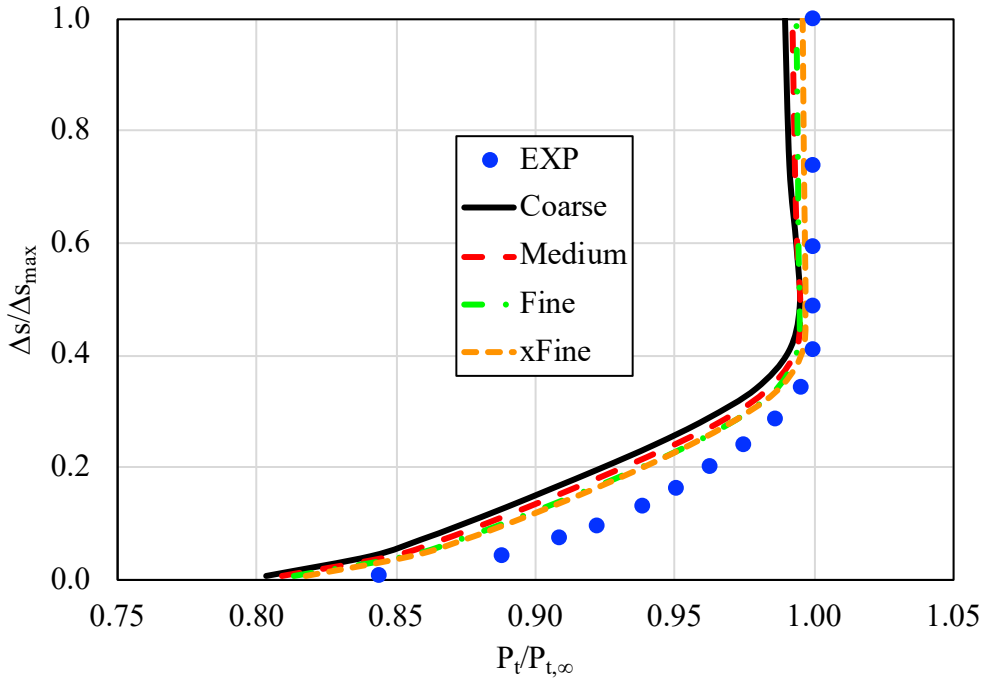

Fig. 24 Total pressure profile comparisons at center rake for Series 11 ($Re_L = 58.45 \times 10^6$, $M = 0.75$).

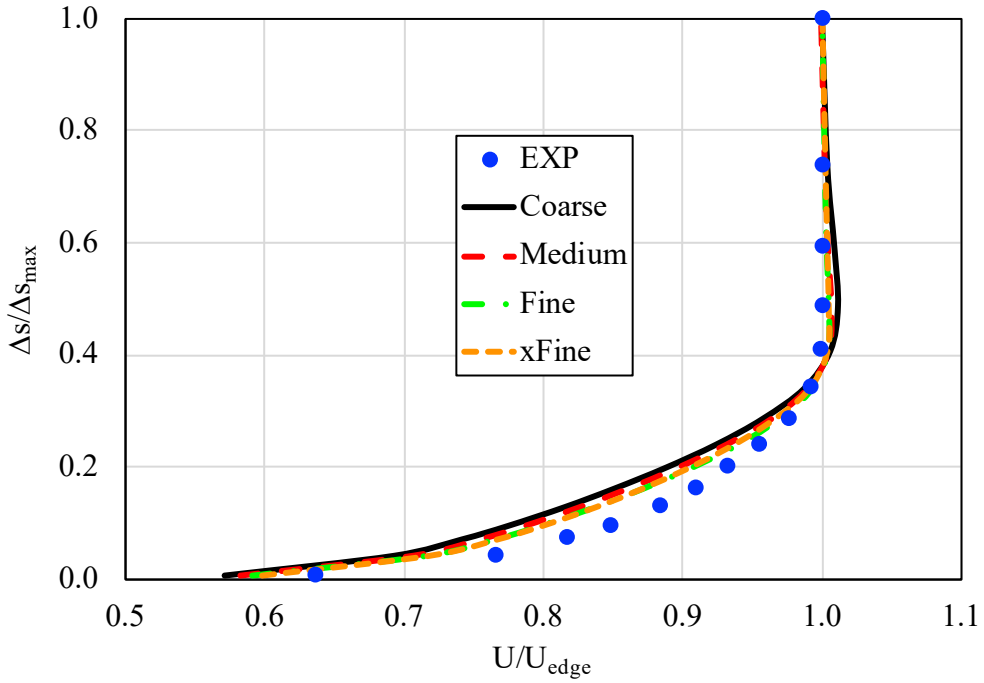

Fig. 25 Velocity profile comparisons at center rake for Series 11 ($Re_L = 58.45 \times 10^6$, $M = 0.75$).

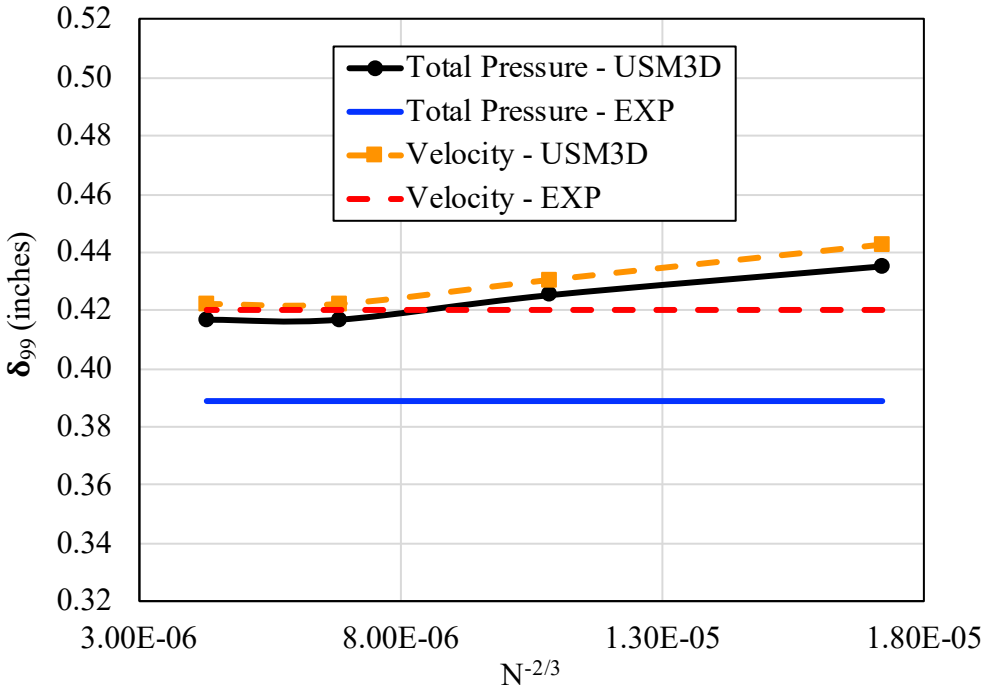

Fig. 26 Calculated boundary layer thickness comparisons for Series 11 ($Re_L = 58.45 \times 10^6, M = 0.75$).

Consistent with the boundary layer profile comparisons, the calculated boundary layer thicknesses from the USM3D predictions agree better to the experiment for the velocity profiles than for the total pressure profiles. This is the opposite of the trend observed from the Series 1 and 5 predictions. The calculated boundary layer thicknesses for Series 11 exhibit a maximum difference of roughly 0.02 inches between the boundary layer thicknesses calculated for the four grid refinements. The difference between the USM3D and experimental values for the boundary layer thicknesses calculated using the total pressure profiles is bounded by roughly 0.03 to 0.05 inches considering all four grid refinements with the trend of decreasing difference with increasing grid resolution. Additionally, the calculated boundary layer thicknesses appear to remain constant between the fine and extra fine grids, which indicates that further refinement is not needed.

VII. Summary and Conclusions

This paper discussed USM3D analyses that were performed in support of a wind tunnel test in the 0.3-Meter Cryogenic Transonic Tunnel at the NASA Langley Research Center. The model that was tested was a semispan fuselage representative of a BLI configuration. The purpose of the test was to assess the impact of various BLTs on the boundary layer height and shape for a nonplanar geometry in high-speed subsonic flow. The USM3D analyses were performed to allow for comparison between the experiment and CFD. The comparisons included surface pressure distributions along the centerline, as well as velocity and total pressure profiles at the boundary layer rakes for two BLT configurations and the baseline configuration. The two BLTs that were considered were the forward facing ramp and the two row, variable height, high density pin configuration. Overall, the comparisons showed that USM3D does a good job predicting the surface pressure distributions for all three configurations. The USM3D predictions for the total pressure boundary layer profiles also show favorable agreement with the experimentally measured values with larger differences observed for the velocity profiles. The differences observed for the velocity profiles were partially attributed to the impact of the boundary layer rakes on the static pressure measured on the surface, which was used to obtain the velocity profiles for the experimental data. The boundary layer profiles predicted by USM3D for both Series 5 and 11 generally exhibit larger differences close to the surface with better agreement further from the surface. Additionally, a grid sensitivity study was performed to assess the impact of grid resolution on the USM3D predictions. The most noteable impacts were a decrease in total pressure losses at the edges of the boundary layer and generally, better agreement between the boundary layer thicknesses predicted by USM3D and the experimental values with increasing grid resolution. The solutions for Series 1 and 11 were shown to exhibit small variation between the grid refinements with relatively good

agreement between the fine and extra fine grids. This was not observed for Series 5, which illustrated significant differences between the fine and extra fine grids that potentially indicates the need for further grid refinement. Finally, the boundary layer thickness calculations were compared to the experimental values as a function of the grid resolution. The boundary layer thicknesses were calculated for both the total pressure and velocity profiles. The results show that the values calculated using the total pressure profiles result in better agreement between USM3D and the experiment for Series 1 and 5. This result is expected since the total pressure values were measured directly in the experiment. However, the calculated thicknesses for the velocity profile was shown to agree to the experiment better for Series 11. Due to discussed issues with the velocity profiles, the boundary layer thickness calculated using the total pressure profiles should be used as the indicator of solution quality for all cases.

The analyses performed for Series 1, 5, and 11 consisted of making comparisons between models in the tunnel where the CFD analyses did not include the boundary layer rakes. The boundary layer rakes are intrusive and will have an impact on the flow as a result. Considering the total pressure comparisons for the baseline configuration in Figure 16, the rake does not appear to have a strong influence. However, the boundary layer rakes were observed to impact the surface pressures and the resulting calculated velocity profiles. Future work will assess the impact of including the boundary layer rakes in the CFD analyses. Additionally, all of the analyses performed for this work employed the SA-QCR turbulence model and the HLLC scheme for computing the inviscid fluxes. Future work will also assess the impact of the turbulence model and inviscid flux schemes on the resulting surface pressure and boundary layer profile predictions.

Acknowledgments

The effort has been supported by the Advanced Air Transport Technology (AATT) project and the Novel Propulsion Airframe Integration (NPAI) team. Special thanks are given to Richard Campbell of NASA Langley for providing the back pressure controller that was used to obtain the target Mach number for the simulations. The authors would also like to thank Mike Park of NASA Langley for his guidance for the task of scaling the boundary layer growth rates for the grid refinement study.

References

[1] Felder, J., Kim, H., and Brown, G., "Turboelectric Distributed Propulsion Engine Cycle Analysis for Hybrid-Wing-Body Aircraft," *47th AIAA Aerospace Sciences Meeting Including The New Horizons Forum and Aerospace Exposition*, 2009. AIAA-2009-1132.

[2] Geiselhart, K. A., Daggett, D. L., Kawai, R., and Friedman, D., "Blended Wing Body Systems Studies: Boundary Layer Ingestion Inlets With Active Flow Control," 2003. NASA/CR-2003-212670.

[3] Welstead, J., and Felder, J. L., "Conceptual Design of a Single-Aisle Turboelectric Commercial Transport with Fuselage Boundary Layer Ingestion," *54th AIAA Aerospace Sciences Meeting*, 2016. AIAA-2016-1027.

[4] Gray, J. S., Mader, C. A., Kenway, G. K., and Martins, J., "Approach to Modeling Boundary Layer Ingestion using a Fully Coupled Propulsion-RANS Model," *58th AIAA/ASCE/AHS/ASC Structures, Structural Dynamics, and Materials Conference*, 2017. AIAA-2017-1753.

[5] Otten III, L., and Van Kuren, J., "Artificial Thickening of High Subsonic Mach Number Boundary Layers," *AIAA Journal*, Vol. 14, No. 11, 1976, pp. 1528–1533.

[6] Jones, G. S., Milholen, W., Elmiligui, A., Bozeman, M., Cramer, C., and Cagle, M., "Artificial Thickening of a Transonic Boundary Layer for the NASA Tail Cone Thruster Boundary Layer Ingestion Concept," *AIAA 2020 SciTech Forum*, 2020.

[7] Klebanoff, P., and Diehl, Z., "Some Features of Artificially Thickened Fully Developed Turbulent Boundary Layers with Zero Pressure Gradient," Tech. rep., NATIONAL BUREAU OF STANDARDS GAITHERSBURG MD, 1951.

[8] Sajben, M., Kroutil, J., Hoffman, G., and Sedrick, A., "Generation of Velocity Profiles using Screens of Nonuniform Solidity," *AIAA Journal*, Vol. 13, No. 4, 1975, pp. 417–418.

[9] Johnson, D. F., and Mitchell, G. A., "Experimental Investigation of Two Methods for Generating an Artificially Thickened Boundary Layer," 1971. NASA-TM-X-2238.

[10] Clever, W. W., et al., "Results of an Experimental Turbulent Boundary Layer Control Investigation," 1969. NASA-TM-X-53099.

[11] Crews, K., "0.3 Meter Transonic Cryogenic Tunnel (0.3M TCT)," , 2018. URL https://researchdirectorate.larc.nasa.gov/0-3-meter-transonic-cryogenic-tunnel-0-3m-tct/.

[12] Allen, B., "Wind Tunnels at NASA Langley Research Center," , 2008. URL https://www.nasa.gov/centers/langley/news/factsheets/windtunnels.html.

[13] "Heldenmesh User Manual, Version 3.03," , 2019.

[14] Frink, N. T., Pirzadeh, S. Z., Parikh, P. C., Pandya, M. J., and Bhat, M., "The NASA Tetrahedral Unstructured Software System TetrUSS," *The Aeronautical Journal*, Vol. 104, No. 1040, 2000, pp. 491–499.

[15] Pandya, M., Frink, N. T., Abdol-Hamid, K. S., Samareh, J. A., Parlette, E. B., and Taft, J. R., "Enhancements to TetrUSS for NASA Constellation Program," *Journal of Spacecraft and Rockets*, Vol. 49, No. 4, 2012, pp. 617–631.

[16] Park, M. A., Campbell, R. L., Elmiligui, A. A., Cliff, S. E., and Nayani, S., "Specialized CFD Grid Generation Methods for Near-Field Sonic Boom Prediction," *52nd Aerospace Sciences Meeting*, 2014. AIAA-2014-0115.

[17] Frink, N. T., "Tetrahedral Unstructured Navier-Stokes Method for Turbulent Flows," *AIAA Journal*, Vol. 36, No. 11, 1998, pp. 1975–1982.

[18] Pandya, M. J., Diskin, B., Thomas, J. L., and Frink, N. T., "Assessment of USM3D Hierarchical Adaptive Nonlinear Method Preconditioners for Three-Dimensional Cases," *AIAA Journal*, 2017, pp. 3409–3424.